Chapter 5

Linear analysis

In this chapter, I present the linearization of the WEM in the conductive range which is for materials with $\epsilon_a < 0$ restricted to relatively low external frequencies. The emphasis lies on approximate analytic results, to see the functional dependence of the various quantities. After several approximations (well-controlled for usual parameter ranges), one arrives at a linear $2\times$ 2 normal form for the amplitudes of the charge-carrier mode and of the critical conductive mode of the SM. Solving this 2×2 equation with the ansatz $e^{\lambda t}$ leads at threshold (Re λ =0) for certain ranges of the system parameters to a nonzero imaginary part ω_H which can be identified as the Hopf frequency. More specifically, the condition for the Hopf bifurcation is $\tilde{r} < R_c\tilde{\alpha}C'$ (where C' is of the order of unity) and if this condition is well satisfied, ($\tilde{r} \leq 0.5R_c\tilde{\alpha}C'$ will do for practical purposes), the Hopf frequency is proportional to $\tilde{\alpha} \propto \sqrt{\mu_\perp^+\mu_\perp^-}$ and has a functional dependence on the external frequency ω_0 depending only on SM parameters.

These predictions are compared with two sets of experiments employing the NLCs MBBA and I 52. The dependence of the Hopf frequency and of the capacitance on ω_0 agrees nearly quantitatively with the experiments and the fit to the frequency of the measured travelling waves gives a geometric mean of the mobilities of about $1.6 \times 10^{-10}\mathrm{m}^2/(\mathrm{Vs})$ for MBBA and of $0.45 \times 10^{-10}\mathrm{m}^2/(\mathrm{Vs})$ for I 52, consistent with the reported data of Table 3.1. The mechanism leading to a Hopf bifurcation is quite similar to that of other periodic-oscillatory pattern-forming systems. This will be discussed by comparing the WEM with three thermal convection systems.

As a "by-product" of this approach, an analytic approximation of the three-dimensional linear stability analysis of the SM, performed some time ago [47, 48], is given in the form of a new, intuitive threshold formula.

Readers not interested in the details of the linearization of the SM and the WEM

(or who are abhorred by longer equations) can start with the 2×2 equations (5.38) in Chapter 5.4, bearing in mind that this system results from the basic equations by applying a Fourier transform in x, y, and in time, a lowest-order Galerkin expansion, and adiabatically eliminating the velocities and the charge density.

5.1 Linearization of the WEM equations

We decompose the fields of the scaled WEM model, Eqs. (3.18) - (3.21) into the basic state Eq. (4.1), denoted by an index 0, and into linearized perturbations, denoted by a superscipt $^{(1)}$. The basic state is a superposition of the trivial basic state (basic state of the SM together with $\sigma = 1$) and of the WEM boundary layers which are denoted by δ,

$$\begin{aligned}
\boldsymbol{E} &= E_0(z,t)\boldsymbol{e}_z - \boldsymbol{\nabla}\phi^{(1)}(\boldsymbol{r},t) &&= [\pi^{-1}\sqrt{2R}\cos\omega_0 t + \delta E_0(z,t)]\boldsymbol{e}_z - \boldsymbol{\nabla}\phi^{(1)}(\boldsymbol{r},t), \\
\rho &= \delta\rho_0(z,t) + \rho^{(1)}(\boldsymbol{r},t) &&= \delta\rho_0(z,t) + \hat{\epsilon}\phi^{(1)} + \epsilon_a E_0 \partial_x n_z^{(1)}, \\
\sigma &= \sigma_0(z,t) + \sigma^{(1)}(\boldsymbol{r},t) &&= 1 + \delta\sigma_0(z,t) + \sigma^{(1)}(\boldsymbol{r},t), \\
\boldsymbol{n} &= (1,0,0) + (0, n_y^{(1)}, n_z^{(1)}), \\
\boldsymbol{v} &= \boldsymbol{v}^{(1)}.
\end{aligned} \tag{5.1}$$

The charge density of the boundary layers is denoted with $\delta\rho_0 = \partial_z \delta E_0$, and $\hat{\epsilon} = -\epsilon'_{ij}(\boldsymbol{n}_0)\partial_i\partial_j = -(\boldsymbol{\nabla}^2 + \epsilon_a\partial_x^2)$. The linearized WEM equations are obtained by inserting the decomposition (5.1) into the Eqs. (3.18) - (3.21) and the BCs (3.23) – (3.26). For a nontrivial basic state, these equations are rather lengthy. They are given for normal rolls in Appendix A.2.

In the following, I assume the trivial SM basic state which is a good approximation if the cell thickness is much larger than the sum of the thicknesses of the two BLs, $2d_{BL} \leq 2\ \mu$m (Chapter 4). Furthermore, I neglect all diffusivity terms, a good approximation if the smallest length scale of the rolls is much larger than the Debye length, $2\pi/|\boldsymbol{q}_c| >> 0.2\ \mu$m , which is always fulfilled in the conductive range. The intrinsic time scale of the velocities, given by the diffusion time τ_{visc} in Table 3.2, is always negligibly small compared to the director relaxation time, so the velocities can be adiabatically eliminated by setting $(\partial_t + \boldsymbol{v}\cdot\boldsymbol{\nabla})\boldsymbol{v}$ equal to zero in the momentum-balance equations.

After a Fourier transform of the linearized WEM fields $\boldsymbol{u}^{(1)} \equiv (\phi^{(1)}, \sigma^{(1)}, n_z^{(1)}, n_y^{(1)}, \boldsymbol{v}^{(1)})$,

$$\boldsymbol{u}^{(1)}(\boldsymbol{r},t) = e^{iq\cdot x}\overline{\boldsymbol{u}}(z,t) + \text{c.c.}, \tag{5.2}$$

the equations of the linearized WEM equations for the charge density, the local conductivity, the director fields n_z and n_y, the z and y components of the curl of the

momentum balance, and the incompressibility condition, are given by

$$
\begin{aligned}
\left[P_1\partial_t\hat{\epsilon}_q+\hat{\sigma}_q\right]\overline{\phi}+E_0\partial_z\overline{\sigma}+\left[P_1\epsilon_a(\dot{E}_0+E_0\partial_t)+\sigma_aE_0\right]iq\overline{n}_z &= 0, \quad (5.3)\\
\left[\tilde{\alpha}^2\pi^2E_0\partial_z-\tilde{d}\partial_t\right]\hat{\epsilon}_q\overline{\phi}+\left[\partial_t+\tilde{r}\right]\overline{\sigma}+\left[\epsilon_a(\tilde{\alpha}^2\pi^2E_0^2\partial_z-\tilde{d}\partial_tE_0)\right]iq\overline{n}_z &= 0, \quad (5.4)\\
-\epsilon_a\pi^2E_0q^2\overline{\phi}+\left[\partial_t+\hat{K}_{zz}-\epsilon_a\pi^2E_0^2\right]iq\overline{n}_z+\hat{K}_{zy}p\overline{n}_y & \\
+\alpha_3iq\partial_z\overline{v}_x+|\alpha_2|q^2\overline{v}_z &= 0, \quad (5.5)\\
-\hat{K}_{zy}ip\overline{n}_z+\left[\partial_t+\hat{K}_{yy}\right]qn_y+\alpha_3iqp\overline{v}_x-|\alpha_2|q^2i\overline{v}_y &= 0, \quad (5.6)\\
\alpha_3p\partial_z\partial_t\overline{n}_z-\left[\alpha_2q^2-\alpha_3p^2\right]\partial_ti\overline{n}_y & \\
-\left[(\eta_0-\eta_1-\alpha_2)q^2+\eta_2(p^2-\partial_z^2)\right]p\overline{v}_x & \\
+\left[\eta_1q^2-(\eta_2-\alpha_3-\alpha_4)p^2-\frac{\alpha_4}{2}\partial_z^2\right]q\overline{v}_y+\left[q(\eta_2-\alpha_3-\frac{\alpha_4}{2})\partial_z\right]ip\overline{v}_z &= 0, \quad (5.7)\\
-\pi^2E_0q^2\hat{\epsilon}_q\overline{\phi}-\left[(\alpha_2q^2+\alpha_3\partial_z^2)\partial_t+\epsilon_a\pi^2E_0^2q^2\right]iq\overline{n}_z & \\
+\alpha_3pq\partial_z\partial_t\overline{n}_y+\left[(\eta_0-\eta_1-\alpha_2)q^2+\eta_2(p^2-\partial_z^2)\right]\partial_ziq\overline{v}_x & \\
+\left[q(\eta_2-\alpha_3-\frac{\alpha_4}{2})\partial_z\right]iqp\overline{v}_y+\left[(\eta_2-\alpha_3-\alpha_4)\partial_z^2+\eta_1q^2+\frac{\alpha_4}{2}p^2\right]q^2\overline{v}_z &= 0, \quad (5.8)\\
iq\overline{v}_x+ip\overline{v}_y+\partial_z\overline{v}_z &= 0, \quad (5.9)
\end{aligned}
$$

where

$$
\begin{aligned}
\hat{\epsilon}_q &= (1+\epsilon_a)q^2+p^2-\partial_z^2, \quad \hat{\sigma}_q=(1+\sigma_a)q^2+p^2-\partial_z^2, && (5.10)\\
\hat{K}_{zz} &= K_{33}q^2+K_{22}p^2-\partial_z^2, \quad \hat{K}_{zy}=(1-K_{22})q\partial_z, &&\\
\hat{K}_{yy} &= K_{33}q^2+p^2-K_{22}\partial_z^2, && (5.11)\\
\eta_1 &= (-\alpha_2+\alpha_4+\alpha_5)/2, \quad \eta_2=(\alpha_3+\alpha_4+\alpha_6)/2, &&\\
\eta_0 &= \alpha_1+\alpha_4+\alpha_5+\alpha_6. && (5.12)
\end{aligned}
$$

The coefficients η_1, η_2, and $\alpha_4/2 := \eta_3$ are sometimes called Miesowicz coefficients and can be measured directly by simple shear experiments (see, e.g., [25]). The BCs at $z = \pm\pi/2$ are

$$\overline{\phi}=\partial_z\overline{\sigma}=\overline{n}_z=\overline{n}_y=\overline{\boldsymbol{v}}=0. \quad (5.13)$$

The SM part of this set is given, with a different scaling, in Eqs. (3.2a-f) of Ref. [48]. The transformations $\phi \to \pi\overline{\phi}$, $\theta \to -i\overline{n}_z$, $\psi \to \overline{n}_y$, $v_{x/y} \to -i\overline{v}_{x/y}$, $v_z \to \overline{v}_z$, $\sqrt{2}/\pi\overline{V}e^{i\omega t} \to \pi E_0$, $\overline{V}^2/\pi^2(1+e^{2i\omega t}) \to \pi^2E_0^2$, $d \to \pi$, $\partial_t \to P_1\partial_t$ in Eq. (3.2a), $\rho_m d^2/\pi^2 \to P_2 \approx 0$, and ϵ_0, $\epsilon_\perp$, $\sigma_\perp$, γ_1, and K_{11} set to unity, brings these equations into our notation.

5.2 Approximate analytic approach

Equations (5.3) - (5.9) with $\pi E_0 = \sqrt{2R}\cos\omega_0 t$ [see Eq. (5.1) for the trivial basic state $\delta \boldsymbol{E}_0 = 0$] represent a linear system with periodic coefficients allowing the Floquet ansatz

$$\overline{\boldsymbol{u}}(z,t) = \tilde{\boldsymbol{u}}(z,\omega_0 t)e^{\lambda(\boldsymbol{q},R)t} = \Sigma_n \tilde{\boldsymbol{u}}^{(n)}(z)e^{[\lambda(\boldsymbol{q},R)+in\omega_0]t}, \tag{5.14}$$

where the Floquet functions $\tilde{\boldsymbol{u}}$ are 2π periodic in the second argument. Of course, there are infinitely many branches $m = 1, 2, ...$ with growth rates $\lambda_m(\boldsymbol{q}, R)$. The special symmetries of the SM (without flexoeffect) lead to a separation of the eigenspace of the SM modes into four orthogonal subspaces, called IA, IB, IIA, IIB in [52, 94]. In class I, ("symmetric"), the fields $\tilde{\phi}, \tilde{n}_z, \tilde{v}_z$ are symmetric in z while the horizontal components of $\tilde{\boldsymbol{n}}$ and $\tilde{\boldsymbol{v}}$ are antisymmetric. In class A ("conductive"), the electric fields $\tilde{\phi}, \tilde{\rho}$, etc. are antisymmetric with respect to a time translation by a half external period, $t \to t + \pi/\omega_0$, and all other fields are symmetric. In class II ("antisymmetric") and B ("dielectric"), the symmetries are opposite. The terms $\propto \tilde{\alpha}$ in the WEM equation (5.4) retain this symmetry separations. The σ field corresponding to the IA modes of the SM is antisymmetric in z and symmetric with respect to the time translation $t \to t + \pi/\omega_0$. The terms $\propto \tilde{d}$ in (5.4) couple the IA to the IIB modes and the IB to the IIA modes. In particular, the ϕ field of the IA mode excites a σ field symmetric in z and antisymmetric with respect to $t \to t + \pi/\omega_0$ which couples back to the ϕ field of the IIB mode of the SM. Like the flexoelectric terms [94], the terms $\propto \tilde{d}$ break both symmetries while retaining the symmetry with respect to a simultaneous reflexion in z and time translation by a half external period. Usually, the terms $\propto \tilde{d}$ are small (see Chapter 3.3) and will be neglected in the following. This corresponds to a linearization of the simpler equations (3.27) – (3.30) together with the fluid equation (3.21) and the BCs (3.26), instead of the Eqs. (3.18)-(3.26).

To obtain analytic results for the conductive regime (where the IA mode has the lowest threshold), I apply to the Floquet functions the "lowest-order Fourier expansion" in time, where only the lowest-order nontrivial IA contributions of each field are retained [48]. The approximation is justified if $\tau_d >> 2\pi/\omega_0 >> \tau_q$ [48] i.e. necessarily $P_1 = \tau_q/\tau_d << 1$, which is usually fulfilled.

After eliminating $\overline{v}_x$ by the incompressibility condition (5.9), the z dependence of each field is approximated by a test function satisfying the symmetries and the BC (which can be seen as a lowest-order Galerkin expansion). Specifically, I represent the fields by the following lowest-order terms of the combined Fourier expansion in t and Galerkin expansion in z,

$$\tilde{\boldsymbol{u}}(z,\omega_0 t) = \sqrt{\frac{2}{\pi}} \begin{pmatrix} \sigma^{(0)} \sin z \\ \cos z(\phi^+ \cos\omega_0 t + \phi^- \sin\omega_0 t) \\ n_z^{(0)} \cos z \\ n_y^{(0)} \sin 2z \\ v_y^{(0)} \sin 2z \\ v_z^{(0)} \sqrt{\frac{\pi}{2}} C_1(z) \end{pmatrix}, \tag{5.15}$$

where ϕ^+ and ϕ^- are defined by (compare Eq. (5.14)) $\phi^+ \cos z = \tilde{\phi}^{(1)} + \tilde{\phi}^{(-1)}$, $\phi^- \cos z = i(\tilde{\phi}^{(1)} - \tilde{\phi}^{(-1)})$, and $C_1(z)$ is the lowest-order Chandrasekhar function [73],

$$C_1(z) = \frac{\cosh(\lambda_1 z)}{\cosh\left(\lambda_1 \frac{\pi}{2}\right)} - \frac{\cos(\lambda_1 z)}{\cos\left(\lambda_1 \frac{\pi}{2}\right)}; \quad \lambda_1 = 1.50562. \tag{5.16}$$

By projecting Eq. (5.3) onto $\cos z e^{\pm i\omega_0 t}$ and the Eqs. (5.4), (5.5), (5.6), (5.7) and (5.8) onto $\sin z$, $\cos z$, $\sin 2z$, $\sin 2z$, and $C_1(z)$, respectively, one obtains a 7×7 eigenvalue system of the form

$$\left[\lambda(\boldsymbol{q},R)\underline{\underline{B}}(\boldsymbol{q},R,\omega_0) - \underline{\underline{L}}(\boldsymbol{q},R,\omega_0)\right](\sigma^{(0)},\phi^+,\phi^-,n_z^{(0)},n_y^{(0)},v_y^{(0)},v_z^{(0)}) = 0 \tag{5.17}$$

for the growth rate $\lambda(\boldsymbol{q},R)$.

Although the above approximations may appear rather crude, they nevertheless lead to quantitatively good results. This is shown in Table 5.1 for the threshold voltage $V_c = V_{c0}\sqrt{R_c^{\mathrm{SM}}}$ and the corresponding wavevectors q_c and p_c resulting from the minimum R_c of the neutral surface $R_0^{\mathrm{SM}}(q,p)$. Compared are the analytic formula for the neutral surface of this work, Eq. (5.21) below, with numerical results, with the formula resulting from the choice of $\sin^2 z$ instead of $C_1(z)$ as test function for v_z, and also with the exactly solvable case of "free" BC [48]. Another possibility consists in representing v_x by a test function, e.g., $\sin 2z$, rather than using the (exact) incompressibility condition [48]. Furthermore, one can express the velocities in terms of the potentials f and g, given as Eq. (2.29), and approximate the z dependence of f and g by the test functions $C_1(z)$ and $\sin 2z$, respectively [95]. The accuracy is similar to Eq. (5.21); the threshold formula contains more projection integrals but the representation of $\boldsymbol{v}$ in terms of f and g is preferable as a starting point for the nonlinear Galerkin analysis. The bottom line is, that it is preferable to satisfy the incompressibility condition exactly but that the choice of test functions is not critical, as long as they satisfy the correct rigid BC (2.31).

Within the Galerkin approximation, the adiabatically eliminated velocities can

Table 5.1: Comparison of different analytic threshold formulas

approximation	MBBA I, $\omega_0\tau_q = 0.5$		MBBA I, $\omega_0\tau_q = 2$		I52, 30°C, $\omega_0\tau_q = 0.5$		
	V_c	q_c	V_c	q_c	V_c	q_c	p_c
Eq. (5.21) (See also [50])	7.205	1.591	30.95	3.114	14.61	1.068	0.734
Ref. [95]	7.375	1.603	33.62	3.24			
Ref. [48]	7.382	1.475	17.66	2.125			
Eq. (5.21) with $\sin^2 z$ for v_z	7.353	1.619	31.70	3.188	14.87	1.072	0.773
free BC	6.244	1.314	28.02	2.779	12.57	0.801	0.708
numerical result	7.171	1.592	31.81	3.15			

then be expressed in terms of "effective viscosities" with the result

$$v_z^{(0)} = \frac{\frac{\pi^2\overline{E}}{\sqrt{2}}\rho^+ + \lambda\left(-a_2 iqn_z^{(0)} + a_2'\frac{\eta_{zy}}{\eta_{yy}}pn_y^{(0)}\right)}{\eta_z^{(\mathrm{eff})}\,q^2}, \tag{5.18}$$

$$iv_y^{(0)} = \frac{p}{q}\frac{\eta_{zy}}{\eta_{yy}}v_z^{(0)} + \frac{\lambda\left(\alpha_3 I_2 ipn_z^{(0)} + (\alpha_3 p^2 - \alpha_2 q^2)n_y^{(0)}\right)}{\eta_{yy}q^3}. \tag{5.19}$$

The effective shear viscosities $\eta_z^{(\mathrm{eff})}$ and η_{yy} and the effective rotational viscosities a_2 and a_2' are given, together with the other "effective" quantities, in Chapter 5.3; $\overline{E} = \sqrt{R}/\pi$ is the rms. of the external field, and ρ^+ is the in-phase part of the oscillatory charge density. The expression for $v_z^{(0)}$ is very intuitive and is reminiscent of the former one dimensional [34] and two dimensional [46] models. For stationary conditions, the time-independent part $\rho^+\overline{E}$ of the volume force is balanced by the viscosity force $\eta_z^{(\mathrm{eff})}\,q^2 v_z^{(0)}$, discussed further in Chapter 5.3. A nonzero director rotation (λ corresponds to ∂_t) leads *via* the orientational viscosities to a further drag onto the fluid which is, again, balanced by the viscous force.

Apart from very thin cells ($d \leq 10$ μm), the charge relaxation time is also much shorter than τ_d ($P_1 << 1$) and the charge variables ϕ^+ and ϕ^- can be adiabatically eliminated as well,

$$\rho^+ = \epsilon_q\phi^+ + \epsilon_a\overline{E}\sqrt{2}iqn_z^{(0)} = -\overline{E}\sqrt{2}\left(\sigma_a^{(\mathrm{eff})}\,iqn_z^{(0)} + \frac{\epsilon_q}{\sigma_q(1+\omega'^2)}\sigma^{(0)}\right), \tag{5.20}$$

where $\epsilon_q = (1+\epsilon_a)q^2 + p^2 + 1$ and $\sigma_q = (1+\sigma_a)q^2 + p^2 + 1$ are the Galerkin projections of the operators $\hat{\epsilon}_q$ and $\hat{\sigma}_q$. The SM part $-\overline{E}\sqrt{2}\sigma_a^{(\mathrm{eff})}\,iqn_z^{(0)}$ with the

effective conductivity $\sigma_a^{(\mathrm{eff})}$, Eq. (5.23), contains the Carr-Helfrich mechanism which will be discussed in the following Chapter 5.3. The second part of Eq. (5.20) describes the charge separation due to the gradients of the total carrier density and gives rise to a second feedback cycle involving the carrier-density mode. This second stabilizing feedback provides the possibility for a nonzero Hopf frequency and will be discussed in Chapter 5.4.

5.3 Carr-Helfrich mechanism and analytic threshold formula

Above a certain (frequency dependent) threshold for the rms value $\sqrt{R}$ of the applied voltage, the growth rate $\lambda(\boldsymbol{q}, R)$ of the fastest-growing branch with a wavevector $\boldsymbol{q} = (q, p)$ crosses zero. This defines the neutral surface $R = R_0(\omega_0, q, p)$. The global minimum of R_0 with respect to q and p defines the critical wavenumbers q_c and p_c and the threshold $R_c = R_0(q_c, p_c)$. Inserting the adiabatically eliminated field inhomogeneity ϕ^+, Eq. (5.20), and the adiabatically eliminated velocities, Eqs. (5.18) and (5.19), into the Galerkin projection of the Eqs. (5.5) and (5.6), and setting $\sigma^{(0)} = 0$ leads to a 2×2 eigenvalue equation of the form $\left[\underline{\underline{B}}(\boldsymbol{q})\lambda + \underline{\underline{L}}(\boldsymbol{q}, R, \omega_0)\right] (n_z^{(0)}, n_y^{(0)}) = 0$ where the components of $\underline{\underline{B}}$ and $\underline{\underline{L}}$ are just numbers (this equation is the SM part of the 3×3 equations in Appendix A.3). Since the SM does not lead to an oscillatory instability, the neutral curve R_0^{SM} is defined by $\lambda = 0$ and the ensuing determinantal condition $\mathrm{Det}[\underline{\underline{L}}(\boldsymbol{q}, R, \omega_0)] = 0$ leads to the result [1]

$$R_0^{\mathrm{SM}} = \frac{K^{(\mathrm{eff})}}{\epsilon_a^{(\mathrm{eff})} + \frac{a_2 \sigma_a^{(\mathrm{eff})}}{\eta^{(\mathrm{eff})}}}, \tag{5.21}$$

with the effective orientational elasticity

$$\begin{aligned} K^{(\mathrm{eff})} &= K_{zz} - \frac{p^2 K_{zy}^2}{q^2 K_{yy}}, \\ K_{zz} &= K_{33} q^2 + K_{22} p^2 + 1, \\ K_{yy} &= K_{33} q^2 + p^2 + 4 K_{22}, \\ K_{zy} &= (1 - K_{22}) q I_2, \end{aligned} \tag{5.22}$$

[1] Here and in the following, the projection integral $I = 0.986$ of $\sqrt{2/\pi}\cos z$ and $C_1(z)$ is set equal to one

the effective anisotropy of the conductivity

$$\sigma_a^{(\mathrm{eff})} = \frac{\sigma_a}{1+\omega'^2}\left(\frac{\epsilon_q}{\sigma_q} - \frac{\epsilon_a}{\sigma_a}\right), \tag{5.23}$$

$$\omega' = \omega_0 \tau_q \epsilon_q / \sigma_q, \tag{5.24}$$

$$\sigma_q = (1+\sigma_a)q^2 + p^2 + 1, \quad \epsilon_q = (1+\epsilon_a)q^2 + p^2 + 1, \tag{5.25}$$

the effective dielectric constant

$$\epsilon_a^{(\mathrm{eff})} = \epsilon_a \left(q^2 + p^2 + 1\right)\left(\frac{\sigma_q^{-1} + \omega'^2 \epsilon_q}{1+\omega'^2}\right), \tag{5.26}$$

the effective orientational viscosity coupling the director to the fluid,

$$a_2 = -\alpha_2 + \alpha_3\left(\frac{1}{q^2} - \frac{\eta_{zy} p^2 I_2}{\eta_{yy} q^3}\right), \tag{5.27}$$

and the effective viscosity

$$\eta^{(\mathrm{eff})} = \frac{\eta_z^{(\mathrm{eff})}}{1 + \frac{p^2 K_{zy}\eta_{zy} a_2'}{q^2 K_{yy}\eta_{yy} a_2}}, \tag{5.28}$$

$$a_2' = -\alpha_2 + \alpha_3\left(\frac{p^2}{q^2} - \frac{\eta_{yy}}{\eta_{zy}}\frac{I_p}{q}\right), \tag{5.29}$$

$$\eta_z^{(\mathrm{eff})} = \eta_{zz} - \frac{p^2 \eta_{zy}^2}{q^2 \eta_{yy}}, \tag{5.30}$$

$$\eta_{zz} = \eta_1 + (\eta_1 + \eta_2 + \alpha_1)\frac{I_1}{q^2} + \frac{\alpha_4}{2}\frac{p^2}{q^2} + \eta_2 \frac{\lambda_1^4 + I_1 p^2}{q^4}, \tag{5.31}$$

$$\eta_{yy} = \eta_1 + (\eta_1 + \eta_2 + \alpha_1)\frac{p^2}{q^2} + \frac{2\alpha_4}{q^2} + \eta_2 \frac{p^4 + 4p^2}{q^4}, \tag{5.32}$$

$$\eta_{zy} = (\eta_1 + \eta_2 + \alpha_1 - \alpha_4/2)\frac{I_p}{q} + \eta_2 I_p \frac{4 + p^2}{q^3}, \tag{5.33}$$

$$\tag{5.34}$$

where η_0, η_1, and η_2 are given in Eq. (5.12). The projection integrals are given by

$$\begin{aligned} I_1 &= -\langle C_1, \partial_z^2 C_1\rangle &&= 1.2465, \\ I_2 &= \tfrac{2}{\pi}\langle \cos z, \partial_z \sin 2z\rangle &&= 0.848, \\ I_p &= \sqrt{\tfrac{2}{\pi}}\langle C_1, \partial_z \sin 2z\rangle &&= 1.1119, \\ \lambda_1^4 &= \langle C_1, \partial_z^4 C_1\rangle &&= 5.1388, \end{aligned} \tag{5.35}$$

where $\langle ... \rangle$ stands for the integration over z from $-\pi/2$ to $\pi/2$.

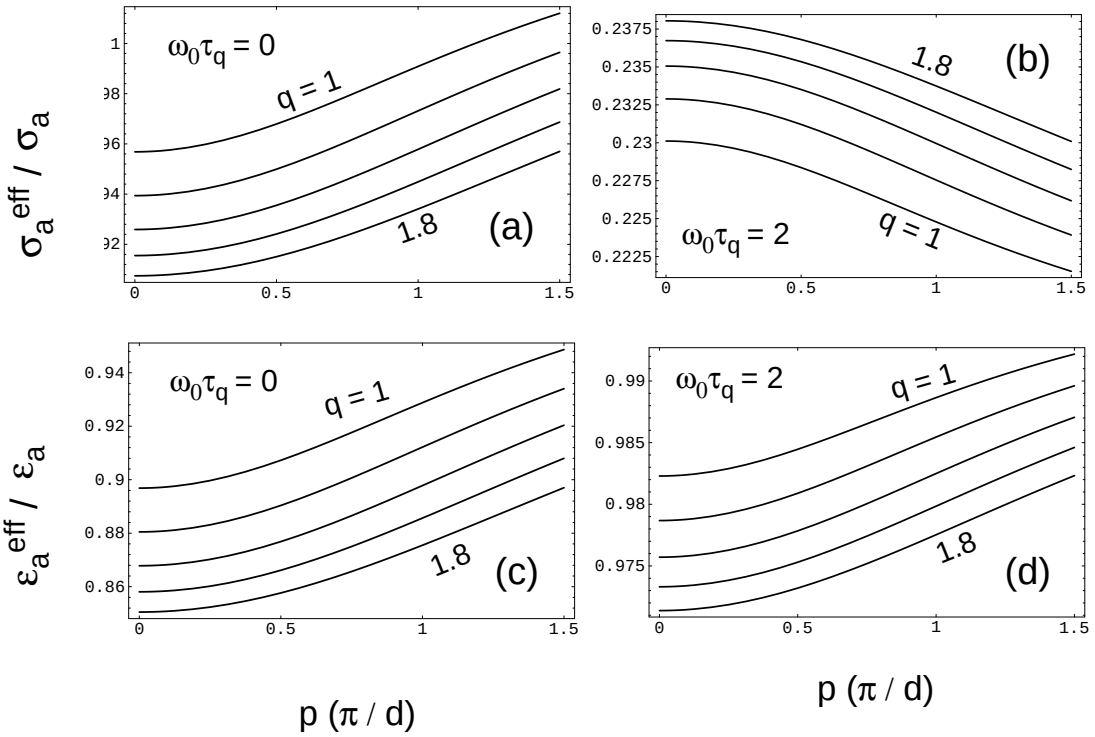

Figure 5.1 The dependence of the effective conductivity anisotropy, Eq. (5.23), and of the effective dielectric anisotropy, Eq. (5.26), on q, p, and ω_0.

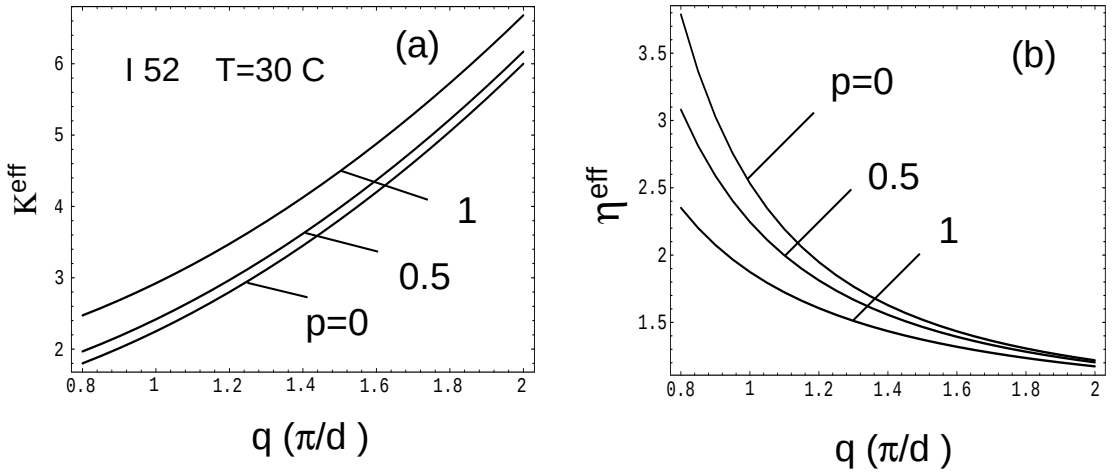

Figure 5.2 (a) The effective orientational elasticity, Eq. (5.22); (b) the effective viscosity, Eq. (5.28). The divergences of $K^{(\mathrm{eff})}$ for $q \to 0$ and of $\eta^{(\mathrm{eff})}$ for $q \to \infty$ lead to a finite, nonzero q_c.

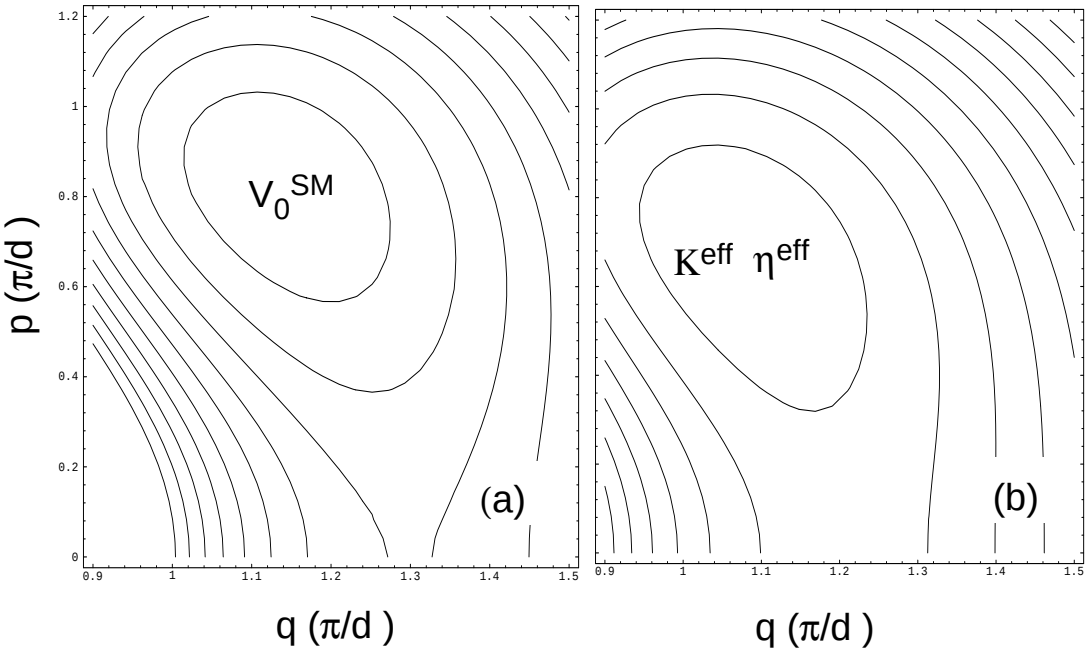

Figure 5.3 Contour plots of (a) the neutral surface, Eq. (5.21), and (b), the product $K^{(\mathrm{eff})}\,\eta^{(\mathrm{eff})}$. The parameters are for I 52 at 30°C. The external frequency $\omega_0\tau_q = 0.5$.

Equation (5.21) is written in such a way that the major effects contributing to the Carr-Helfrich mechanism are separated out. $K^{(\mathrm{eff})}$ describes the elastic torque on the director, which, at threshold, is balanced by the electric forces due to charge accumulation $\propto \sigma_a^{(\mathrm{eff})}\,\overline{E}^2$ and due to the dielectric anisotropy, $\propto \epsilon_a^{(\mathrm{eff})}\,\overline{E}^2$.

For $\epsilon_a < 0$, the dielectric energy has a minimum for $\boldsymbol{n}\cdot\boldsymbol{E} = 0$. The main contribution of the dielectric torque, $\epsilon_a\pi^2 E_0^2(t) i q \overline{n}_z$ in Eq. (5.5), tends to align the director perpendicular to the undistorted electric field. Additional contributions due to field distortions ($\boldsymbol{\nabla}\phi \neq 0$) lead, in the lowest-order Fourier and Galerkin expansions, to a total dielectric torque $\epsilon_a^{(\mathrm{eff})}\,\pi^2\overline{E}^2 i q n_z^{(0)}$ thus defining $\epsilon_a^{(\mathrm{eff})}$. As shown in Fig. 5.1, $\epsilon_a^{(\mathrm{eff})}$ is essentially equal to ϵ_a for all q, p, and ω_0. For $\epsilon_a < 0$, this contribution is stabilizing.

With the help of the Eqs. (5.18) and (5.20), the dominant contribution of the Carr-Helfrich part $|\alpha_2|q^2\overline{v}_z$ of the director equation Eq. (5.5) with v_z can be written as

$$\gamma^{(\text{Carr Helfrich})} = \frac{a_2\sigma_a^{(\mathrm{eff})}\,\pi^2\overline{E}^2 i q n_z^{(0)}}{\eta^{(\mathrm{eff})}}. \tag{5.36}$$

$\gamma^{\text{Carr Helfrich}}$ is an electrically induced torque onto the director that acts indirectly *via* the fluid (compare the Figs. 5.4 and 5.12): A director bend leads *via* the conducti-

vity anisotropy to a divergence of the electric current (with the main contribution $\sigma_a E_0(t) iq\overline{n}_z$ in Eq. (5.3)), which gives rise to a charge accumulation and to a volume force $\rho \boldsymbol{E}$ onto the fluid. In the lowest-order of the Fourier expansion in t, only the part $\propto \rho^+ \overline{E}$ of the volume force not oscillating with the electric field, and deriving from the in-phase part of the accumulated charge density, sets the fluid into motion. So I defined $\sigma_a^{(\mathrm{eff})}$ to be proportional to the SM part of Eq. (5.20), $\rho^+ = -\sigma_a^{(\mathrm{eff})}\, \overline{E}\sqrt{2} iq n_z^{(0)}$. In the stationary case, the non-oscillating part $-\sigma_a^{(\mathrm{eff})}\, \overline{E}^2 \pi^2 iq n_z^{(0)}$ of the volume force is balanced by the viscous forces of the rotating fluid which can be written as $\eta_z^{(\mathrm{eff})}\, q^2 v_z^{(0)}$ thus defining $\eta_z^{(\mathrm{eff})}$. The velocity gradients of the fluid lead *via* the rotational viscosities to a torque onto the director which I wrote as $-a_2 q^2 v_z^{(0)}$ defining a_2. For $\alpha_3 = 0$ ($a_2 = -\alpha_2$), and with the Fourier and Galerkin approximations, this is just the contribution $\alpha_2 q^2 \overline{v}_z$ in Eq. (5.5). With $v_z^{(0)} = -\sigma_a^{(\mathrm{eff})}\, \pi^2 \overline{E}^2 iq n_z^{(0)} / (\eta_z^{(\mathrm{eff})}\, q^2)$, this contribution is equal to Eq. (5.36) with $\eta^{(\mathrm{eff})}$ substituted by $\eta_z^{(\mathrm{eff})}$. In addition, the total destabilizing Carr-Helfrich contribution (5.36) of the torque contains the Fourier and Galerkin approximations of the coupling term $-\hat{K}_{zy} p \overline{n}_y$ in Eq. (5.5). This term can be put formally into the definition of $\eta^{(\mathrm{eff})}$ leading to the difference between $\eta^{(\mathrm{eff})}$ and $\eta_z^{(\mathrm{eff})}$.

The fact that only the in-phase part of ρ is relevant, leads to the denominator $(1 + \omega'^2)$ in Eq. (5.23) for $\sigma_a^{(\mathrm{eff})}$ making the Carr-Helfrich effect less effective for increasing external frequencies ($\eta^{(\mathrm{eff})}$ in Fig. 5.1). On the other hand, the effective viscosity decreases monotonically with increasing q (Fig. 5.2) approaching the asymptotic value $\eta_1 = (\alpha_4 + \alpha_5 - \alpha_2)/2$ for $q \to \infty$ and making this aspect of the Carr-Helfrich mechanism more effective for large wave numbers. [2] This explains the increase of the critical wavenumber q_c with increasing ω_0, and the existence of a "cutoff frequency" for $\epsilon_a < 0$. On increasing ω_0, the strength of the Carr-Helfrich effect decreases due to the decrease of $\sigma_a^{(\mathrm{eff})}$; to overcome the stabilizing and essentially q and ω_0 independent dielectric effect ($\epsilon_a^{(\mathrm{eff})}$ in Fig. 5.1), q_c increases with increasing ω_0. The effective viscosity, however, remains finite for $q \to \infty$. As a result there exists, for $\epsilon_a < 0$, a finite cutoff frequency ω_{cutoff} [45], where the Carr-Helfrich mechanism cannot overcome the dielectric force even for $q \to \infty$ and where R_c^{SM} diverges for the conductive mode. For a discussion, see, e.g., Ref. [48].

In general, $\eta^{(\mathrm{eff})}$ decreases with the roll angle $\arctan(p/q)$ for constant q (Fig. 5.2) while the behaviour of $\sigma_a^{(\mathrm{eff})}$ depends on the external frequency. For low (high)

[2] For a negative Miesowicz coefficient $\eta_2 = (\alpha_3 + \alpha_4 + \alpha_6)/2$, the effective viscosity would become negative for q values *smaller* than some q_{min}. Note, however, that positive definiteness of the entropy production (2.17) leads to the Miescowicz coefficient $\eta_2 > 0$ [58] and forbids this unphysical behaviour.

external frequencies, $\sigma_a^{(\mathrm{eff})}$ increases (decreases) favouring oblique (normal) rolls, see Fig. 5.1. For some NLCs (I 52, but not MBBA), the product of the restoring forces $K^{(\mathrm{eff})}\,\eta^{(\mathrm{eff})}$ has a minimum for nonzero p_c (Fig. 5.3). In I 52, this leads to oblique rolls except for very high frequencies where $\sigma_a^{(\mathrm{eff})}$ strongly favours normal rolls.

For $q = 0$, Eq. (5.21) becomes $R_0^{\mathrm{SM}} = K^{(\mathrm{eff})}/\epsilon_a$ which is positive (i.e. corresponds to a threshold) for $\epsilon_a > 0$. Usually, the effective restoring force $K^{(\mathrm{eff})}$ increases with p and the minimum of $R_0^{\mathrm{SM}}(q = 0, p)$ lies at $p = 0$ corresponding to the usual Fréedericksz effect. If the value of the twist module is extremely low, $K_{22}/K_{33} < 0.298$, [3] the minima of $K^{(\mathrm{eff})}\,(q = 0, p)$ and of $R_0^{\mathrm{SM}}(q = 0, p)$ are at a nonzero wave number p corresponding to the "periodic splay-twist transition", as decsribed e.g., in Ref. [48].

5.4 Charge separation mechanism and Hopf frequency

5.4.1 Coupled equations for the director bend and the charge-carrier density

As in Chapter 5.3, I substituted the adiabatically eliminated ϕ^+, Eq. (5.20), and the adiabatically eliminated velocities, Eqs. (5.18) and (5.19), into the Galerkin projection of the linear basic equations (5.4), (5.5) and (5.6), but this time I retain the amplitude $\sigma^{(0)}$ of the charge-carrier-density mode. This leads to a 3×3 eigenvalue system for the linear growth rate λ with the eigenvector $\left(\sigma^{(0)}, n_z^{(0)}, n_y^{(0)}\right)$ which is given explicitly in the Appendix A.3.

Near threshold, where the reduced control parameter

$$\epsilon = \frac{R}{R_c} - 1 \tag{5.37}$$

satisfies $\epsilon << 1$, this system can be further reduced systematically to a 2×2 normal form for the amplitude $A_n(t)$ of the SM mode and the amplitude $A_\sigma(t)$ of the charge-carrier mode (see Appendix A.3),

$$\begin{aligned} \partial_t A_\sigma &= \lambda_\sigma(R) A_\sigma - \tilde{\alpha}^2 R \sigma_a^{(\mathrm{eff})}\, A_n, \\ \partial_t A_n &= \frac{R}{\sigma_a^{(\mathrm{eff})}} \left(\frac{C}{1+\omega'^2}\right)^2 A_\sigma + \lambda_n(R) A_n. \end{aligned} \tag{5.38}$$

[3] This value is the result for the Galerkin approximations. The problem is exactly solvable with the result $K_{22}/K_{33} < (\beta_0^2 + \beta_0)^{1/2} - \beta_0 = 0.303$ with $\beta_0 = \pi^2/8 - 1$ [96].

The critical SM mode $A_n(t)$ is the amplitude of the director bend with a small admixture of twist,

$$\begin{pmatrix} iq\overline{n}_z(z,t) \\ q\overline{n}_y(z,t) \end{pmatrix} = \begin{pmatrix} \cos z \\ \alpha_n \sin 2z \end{pmatrix} A_n(t), \tag{5.39}$$

where $\alpha_n = in_z^{(0)}/n_y^{(0)}$ is given by the eigenvector of the 3×3 system (A.5) - (A.7). The charge-carrier mode is given by

$$\overline{\sigma}(z,t) = A_\sigma(t) \sin z. \tag{5.40}$$

Neglecting some small terms $\propto \alpha_3 p$, the growth rates λ_σ and λ_n of the charge-carrier and SM modes, and the coupling coefficient C, are given by [4]

$$\lambda_\sigma = -\left(\tilde{r} + \frac{\tilde{\alpha}^2 R \epsilon_q}{\sigma_q(1+\omega'^2)}\right) \approx -\tilde{r}, \tag{5.41}$$

$$\lambda_n = \frac{\epsilon}{\tau_0^{\rm SM}}, \tag{5.42}$$

$$C^2 = \frac{K_{zz}}{K^{(\rm eff)}\,|\lambda_{0z}|\tau_0^{\rm SM}} \left(C_z^2 + \frac{p^2 K_{zy}\lambda_{0z}}{q^2 K_{zz}\lambda_{0y}} C_y^2\right), \tag{5.43}$$

$$C_z^2 = \frac{\sigma_a \epsilon_q^2 |\lambda_{0z}|}{\sigma_q^2 \eta_z^{(\rm eff)}\, K_{zz}} \left(1 - \frac{\epsilon_a}{\epsilon_q}\frac{\sigma_q}{\sigma_a}\right)\left(a_2 - \frac{\epsilon_a q^2 \eta_z^{(\rm eff)}}{\epsilon_q}\right), \tag{5.44}$$

$$C_y^2 = \frac{\sigma_a \epsilon_q^2 |\lambda_{0y}|}{\sigma_q^2 \eta_z^{(\rm eff)}\, K_{yy}} \left(1 - \frac{\epsilon_a}{\epsilon_q}\frac{\sigma_q}{\sigma_a}\right)\frac{\eta_{zy}}{\eta_{yy}} a_2', \tag{5.45}$$

and the zero-field growth rates λ_{0z} and λ_{0y} are given by

$$\lambda_{0z} = -\frac{K_{zz}\eta_z^{(\rm eff)}}{\eta_z^{(\rm eff)} - a_2^2}, \quad \lambda_{0y} = -\frac{K_{yy}\eta_z^{(\rm eff)}}{\eta_z^{(\rm eff)}\left(1 - \frac{a_2'^2}{\eta_{yy}}\right) - \frac{p^2}{q^2}\frac{\eta_{zy}^2}{\eta_{yy}^2} a_2'^2}. \tag{5.46}$$

For normal rolls $K^{(\rm eff)} = K_{zz}$ and $\tau_0^{\rm SM} = -1/\lambda_{0z}$ so that $C^2 = C_z^2$ is equivalent to the normal-roll expression in Ref [92], if one identifies $\eta_z^{(\rm eff)}$ with $1/L_{nn}$. [5] The question may arise whether the denominators proportional to $(\eta_z^{(\rm eff)} - a_2^2)$ in the growth rate λ_{0z} (and thus in C_z^2) can become zero or negative leading to unphysical results. This question is most critical for $q \to \infty$ and $p = 0$ (Fig. 5.2), where, in physical

[4] Due to a different scaling of the voltages and the time, the definition of C differs from that used in the Refs. [92] and [42] by a factor of $(\sigma_a/\sigma_\perp^{\rm eq})^{1/2}$.

[5] There is a printing error in Eq. (38) of Ref. [92]. The factor $(1 - \frac{\epsilon_a}{\epsilon_q} L_{nn} q^2)$ should be replaced by $(L_{nn} - \frac{\epsilon_a}{\epsilon_q} q^2)$.

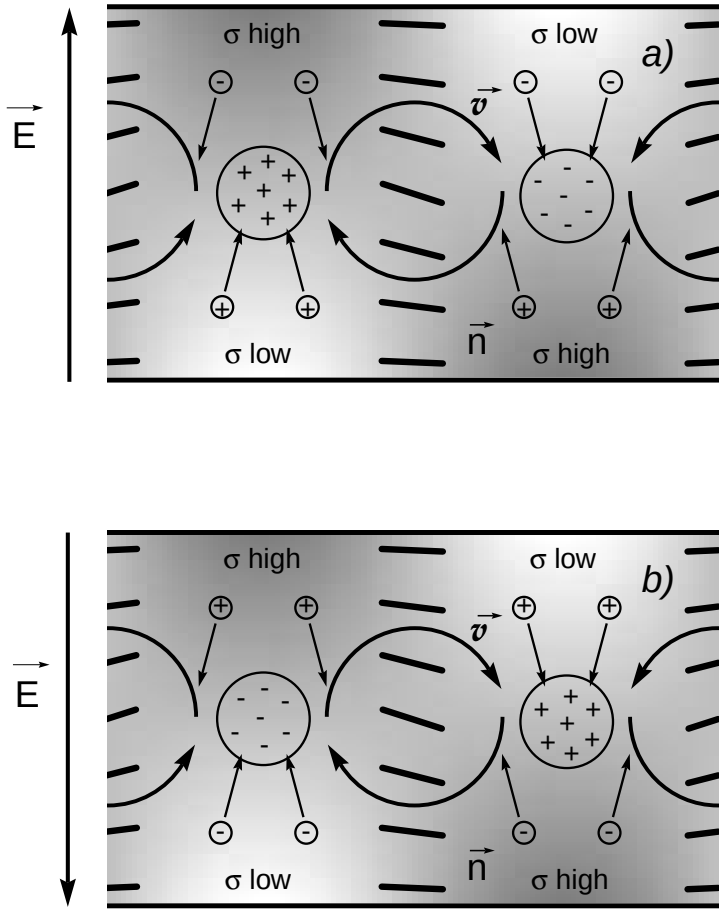

Figure 5.4 Sketch of the spatial distribution of the physical quantities inside the nematic layer (conductive regime). The straight arrows indicate the contributions to the current carried by each species. The shading illustrates the charge-carrier mode (dark = σ high, light = σ low).

units, $\eta_1 > \alpha_2^2/\gamma_1$ is required to avoid unphysical results. It can be shown that the requirement of a positive fluid contribution $-T_{ij}^D \partial_j v_i$ of the entropy production (2.17) leads indeed to $\eta_1 > \alpha_2^2/\gamma_1$ [6]

5.4.2 The dynamics of the charge-carrier mode

The charge-separation mechanism of the WEM leading for low recombination rates to a nonzero Hopf frequency, can be explained essentially with the help of Fig. 5.4, Eq. (5.20) for the adiabatically eliminated charge density, and the 2×2 system (5.38). Like the Carr-Helfrich effect, this mechanism is active also for DC.

Consider $E_0 > 0$ and a region in the cell where the director bend A_n is negative which is connected by Eqs. (5.20) and (5.39) to a positive SM part of the charge density (left side of upper picture in Fig. 5.4). For $z > 0$, the gradient of the density

[6] The contribution $\eta_1 - \alpha_2^2/\gamma_1$ is sometimes called η_3, e.g., in Ref. [58].

of the upwards drifting positive carriers is negative and that of the downwards drifting negative carriers is positive. Migration of both species leads, for $z > 0$, to an increase in the total number density $\sigma(\boldsymbol{r}, t)$ of the carriers, illustrated by the shading (dark corresponds to a high density). The sign of the effect (accumulation or depletion of the carriers) depends on the signs of $\partial_z \rho$ and E_0. This means, in the conductive regime, that the excited charge-carrier density mode $\sigma(\boldsymbol{r}, t)$ is antisymmetric in z and does not follow the external oscillations in the lowest-order Fourier expansion in t (compare the upper and lower part of Fig. 5.4). This justifies the ansatz (5.15) for the σ mode and Eq. (5.40) for the amplitude A_σ. Within the ansatz (5.15), the driving force for the A_σ mode is proportional to ρ^+, $\partial_t A_\sigma = \tilde{\alpha}^2 \pi^2 \overline{E} \rho^+ / \sqrt{2}$. The SM part of Eq. (5.20) for the adiabatically eliminated ρ^+ leads to the term $-\tilde{\alpha}^2 R \sigma_a^{(\mathrm{eff})} A_n$ in the upper line of Eq. (5.38). The WEM part leads to the part $\propto \tilde{\alpha}^2$ in Eq. (5.41) for the relaxation of the σ mode.

The stabilizing feedback of the A_σ mode on the charge density and on A_n is mediated, in the basic equation (5.4), by the WEM part $E_z \partial_z \overline{\sigma}$ of the divergence of the current. Together with the relaxational part it decreases the accumulated charge. With adiabatically eliminated charge density and velocities, this is equivalent to a decrease of all SM fields, and the WEM part of $\boldsymbol{\nabla} \cdot \boldsymbol{J}$ leads to the first term in the equation for $\partial_t A_n$. This term is positive, but since the director bend A_n is proportional to $-\rho^+$, the feedback is indeed negative, i.e., stabilizing. It leads to a nonzero Hopf frequency, provided the A_σ mode can build up sufficiently, i.e. the relaxation of the σ mode is sufficiently slow. [7]

5.4.3 Hopf frequency and threshold shift

The growth rates of modes $\propto e^{\lambda t}$ in (5.38) are given by

$$\lambda = \frac{\lambda_\sigma + \lambda_n}{2} \pm \sqrt{\frac{(\lambda_n - \lambda_\sigma)^2}{4} - \tilde{\omega}^2} \tag{5.47}$$

with

$$\tilde{\omega} = \frac{R_c \tilde{\alpha} C}{1 + \omega'^2}. \tag{5.48}$$

The condition for a Hopf bifurcation at threshold ($Re\lambda = 0$, $Im\lambda = \pm\omega_H \neq 0$) are

[7] To put it anthropomorphically for normal rolls: If the A_σ mode builds up sufficiently, it is more advantageous for the Carr-Helfrich mechanism if the SM fields were shifted to the left or to the right. The travelling velocity (proportional to the Hopf frequency) is determined by the rate at which the A_σ mode can build up at the new location. This rate is proportional to $\tilde{\alpha}$.

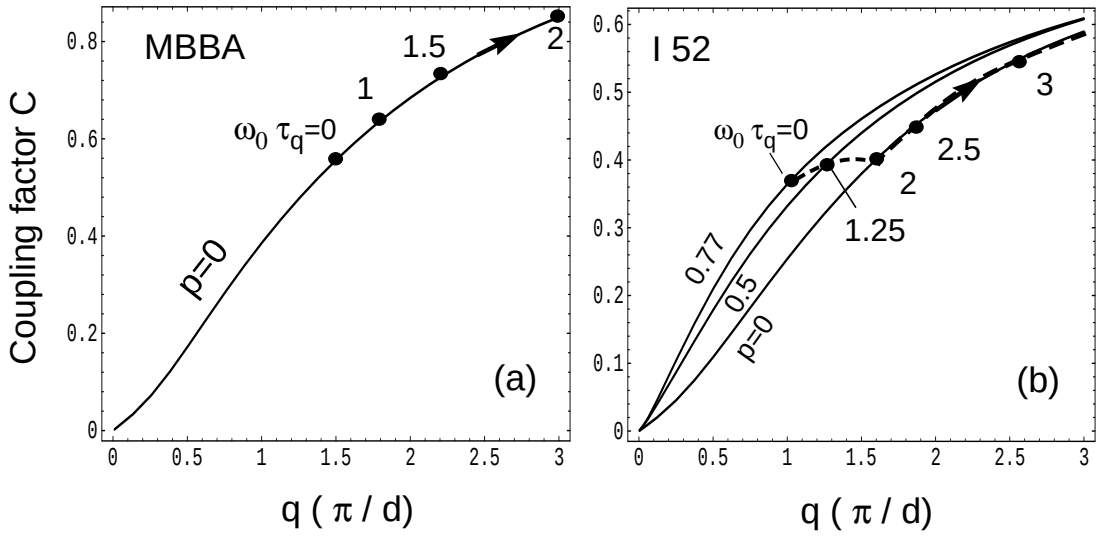

Figure 5.5 Plot of Eq.(5.43) for the coupling factor C in the 2×2 equations (5.38). (a) is for MBBA parameters and $p_c = 0$. The dots on the curve give, for $\omega_0 \tau_q = 0, 1.0, 1.5,$ and 2, the actual value of q_c where C is calculated. The three curves in (b) are for I 52 at 30°C with p_c values corresponding to $\omega_0 \tau_q = 0$, 1.25, and with $p_c = 0$ corresponding to $\omega_0 \tau_q > 2.0$. The kink at the Lifshitz point $\omega_{\rm lif} \tau_q = 2.0$ in the dashed trajectory in (b) translates into a kink in the curves for the Hopf frequency in Fig 5.11a). The slope $\frac{\partial C}{\partial q}$ is the main contribution to the group velocity $\frac{\partial \omega}{\partial q}$.

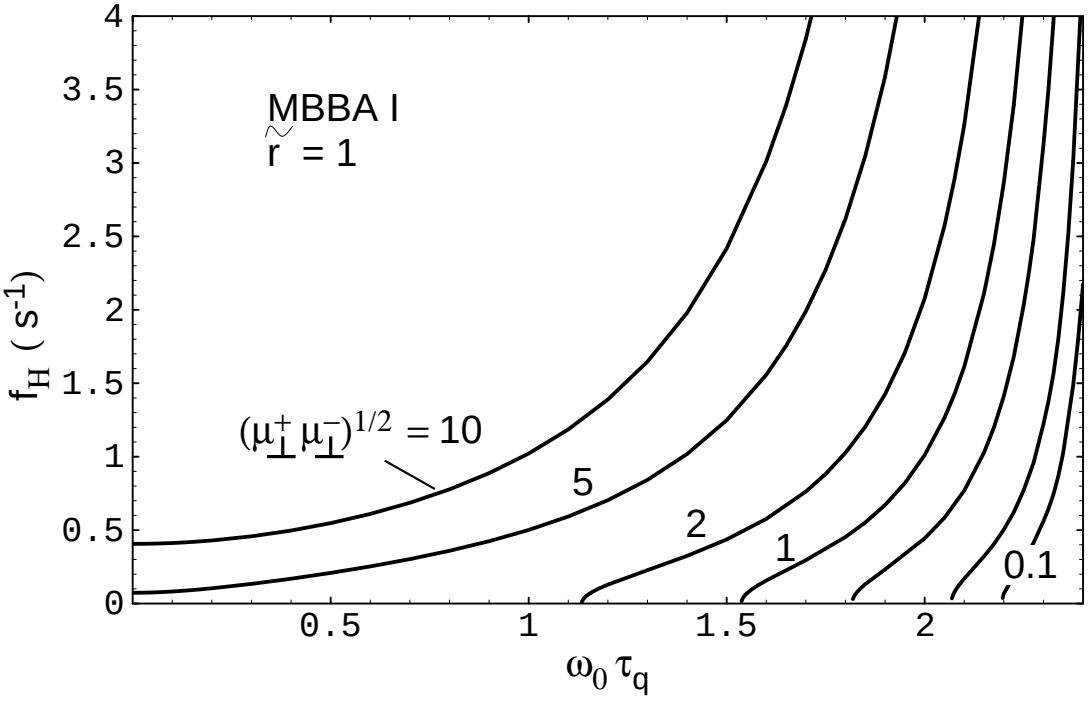

Figure 5.6 Hopf frequency $f_H = (2\pi)^{-1}\omega_H$ in physical units, Eq. (5.53), as a function of the external frequency for the parameter set of MBBA I with $\sigma_\perp = 10^{-8}(\Omega\mathrm{m})^{-1}$ and $d = 13\ \mu$m (as in Ref. [39]), and an assumed recombination rate of $\tau_{\mathrm{rec}} = \tau_d$ (i.e., $\tilde{r} = 1$). Parameter is the geometric mean of the mobilities with the values, from left to right, $10, 5, 2, 1, 0.5, 0.2$, and 0.1 in units of $10^{-10}\mathrm{m}^2/(\mathrm{Vs})$. For other values of d, $\sigma_\perp$, $\sqrt{\mu_\perp^+\mu_\perp^-}$, and τ_{rec}, the form of the curves (especially the codimension-two point where $\omega_H \to 0$) scales with $\tau_{\mathrm{rec}}\tilde{\omega}^{\mathrm{phys}} \propto \tilde{\alpha}/\tilde{r} \propto \sqrt{\mu_\perp^+\mu_\perp^-}\tau_{\mathrm{rec}}/(\sqrt{\sigma_\perp}d^3)$, and the Hopf frequency scales with $\sqrt{\mu_\perp^+\mu_\perp^-}/(\sqrt{\sigma_\perp}d^3)$.

$\lambda_n = -\lambda_\sigma$ and $|\lambda_\sigma| < \tilde{\omega}$ which sets an upper bound on the recombination rate. The resulting Hopf frequency is

$$\omega_H = \tilde{\omega}\sqrt{1 - \left(\frac{\lambda_\sigma}{\tilde{\omega}}\right)^2} \approx \tilde{\omega}\sqrt{1 - \left(\frac{\tilde{r}}{\tilde{\omega}}\right)^2}, \tag{5.49}$$

and the condition $\lambda_n = -\lambda_\sigma$ leads to a threshold shift

$$\Delta\epsilon \equiv \frac{R_c}{R_c^{\rm SM}} - 1 = \begin{cases} |\lambda_\sigma|\tau_0^{\rm SM} \approx \tilde{r}\tau_0^{\rm SM} & |\lambda_\sigma| \le \tilde{\omega} \\ \frac{\tilde{\omega}^2\tau_0^{\rm SM}}{|\lambda_\sigma|} \approx \frac{\tilde{\omega}^2\tau_0^{\rm SM}}{\tilde{r}} & |\lambda_\sigma| > \tilde{\omega} \end{cases}, \tag{5.50}$$

where all quantities are taken at threshold. The only source for a shift of the wave vector with repect to the SM model lies in the q dependence of λ_σ which is proportional to $\tilde{\alpha}^2$ and extremely small, in accordance with experiments [39], see also Chapter 6.3.3.

The approximations in the Eqs. (5.49) and (5.50) are valid for $R_c\tilde{\alpha}^2/(1+\omega'^2) << \tilde{r}$. For the I 52 experiments, $R_c\tilde{\alpha}^2/(1+\omega'^2)$ is of the order of 0.01 or smaller and $\tilde{\omega}$ is of the order of 0.2; so there exists a fairly large range where this approximation is fulfilled.

For $\epsilon_a = \alpha_3 = p = 0$, the expression (5.48) for $\tilde{\omega}$ simplifies to

$$\tilde{\omega}\tau_0^{\rm SM} = \tilde{\alpha}\sqrt{(\eta_{zz} - 1)/\sigma_a}. \tag{5.51}$$

5.4.4 Dependence on the system parameters

The Equations (5.48) – (5.50) are the main analytic result of this Chapter. Apart from the SM parameters, they contain the mobility parameter $\tilde{\alpha}$ and the recombination rate $\tilde{r}$ in units of the inverse director relaxation time. In physical units, the Eqs. (5.48) and (5.49) read (in the approximation $\lambda_\sigma << \tilde{r}$)

$$\tilde{\omega}^{\rm phys} = \pi C\frac{\epsilon_0\epsilon_\perp}{d^3}\frac{\overline{V}^2}{1+\omega'^2}\sqrt{\frac{\mu_\perp^+\mu_\perp^-}{\gamma_1\sigma_a^{\rm eq}}}, \tag{5.52}$$

$$\omega_H^{\rm phys} = \tilde{\omega}^{\rm phys}\sqrt{1 - \frac{1}{(\tau_{\rm rec}\tilde{\omega}^{\rm phys})^2}}. \tag{5.53}$$

while Eq. (5.50) is valid for physical units as well. This implies the following predictions.

- The Hopf condition scales with $d^{-3}(\sigma_\perp^{\rm eq})^{-1/2}$. This means, that a Hopf bifurcation is favoured for thin cells and low conductivities, i.e. for clean materials and/or low temperatures. If the condition is (fairly) well satisfied, the Hopf frequency scales with $d^{-3}(\sigma_\perp^{\rm eq})^{-1/2}$ as well.

- If the Hopf condition is well satisfied, the Hopf frequency $\omega_H \approx \tilde{\omega}$ depends only on one combination of non-SM parameters , $\sqrt{\mu_\perp^+ \mu_\perp^-}$, and this dependence is of a simple multiplicative form. Actually, as shown in the inset of Fig. 5.8, the influence of the recombination can be neglected (i.e. the Hopf condition is "well satisfied") if $\tilde{r}$ is smaller than about half the Hopf frequency for zero external frequency. One could, at least in principle and when the SM parameters are known, "measure" the geometric mean of the mobilities by measuring the Hopf frequency.

- The function $\tilde{\omega}(\omega_0)$ is proportional to $C(q(\omega_0))R_c(\omega_0)/(1+\omega'^2)$, a fixed function for a given NLC at a given temperature containing only SM parameters. The dependence on C is rather weak, so the behaviour of $\tilde{\omega}$ with ω_0 is primarily determined by the factor $R_c/(1+\omega'^2)$. This factor is nearly constant for $\epsilon_a = 0$ (compare Eq. (5.21) with $R_c \approx R_c^{\mathrm{SM}}$), but increases (decreases) with ω_0 for $\epsilon_a < 0$ ($\epsilon_a > 0$). For $\epsilon_a = \alpha_3 = p = 0$, Eq. (5.51) implies that $\tilde{\omega}$, in units of the zero-field relaxation rate $(\tau_0^{\mathrm{SM}})^{-1}$ of the director, is equal to $\tilde{\alpha}\sqrt{\sigma_\perp/\sigma_a}$ times a factor of the order of unity (see Fig. 5.2). This order-of-magnitude estimate remains valid for nonzero values of ϵ_a, α_3, and p.

- The threshold shift increases with $\tilde{r}$ to a maximum of $\Delta\epsilon = \tau_0^{\mathrm{SM}}\tilde{\omega}$ at the codimension-two point ($|\lambda_\sigma| = \tilde{\omega}$) of travelling rolls and stationary rolls ($\Delta\epsilon \approx$ 3 % for I 52.) For higher $\tilde{r}$ (stationary-roll regime), the shift $\Delta\epsilon = \tau_0^{\mathrm{SM}}\tilde{\omega}^2/\tilde{r}$ decreases and goes to zero in the SM limit $\tilde{r} \to \infty$.

5.5 Comparison with experiments

5.5.1 Travelling normal rolls in MBBA

Travelling rolls in MBBA were observed e.g., in [40, 41, 97, 98]. The advantage of MBBA for testing the WEM is the fact that all SM parameters are known and there exist also some reported data for the mobilities (Table 3.1). In this subsection I test the WEM on the results of Rehberg, Rasenat, and Steinberg [41]. The thickness of the cell was $d = 15\ \mu$m and the cutoff frequency at about 450 Hz corresponds to $\sigma_\perp = 4 \times 10^{-8}(\Omega\mathrm{m})^{-1}$. Their Fig. 4, containing the results of the Hopf-frequency measurements, is reproduced here as Fig. 5.7 (Courtesy of I. Rehberg). Travelling waves were observed for all frequencies. Comparison with the inset of Fig. 5.8 suggests that the unknown recombination rate is sufficiently small ($\tilde{r} < 0.3$ or $\tau_{\mathrm{rec}}^{-1} < 0.3\tau_d^{-1}$) to assume $\omega_H = \tilde{\omega}$. Another experiment described in Chapter 6 [39] leads

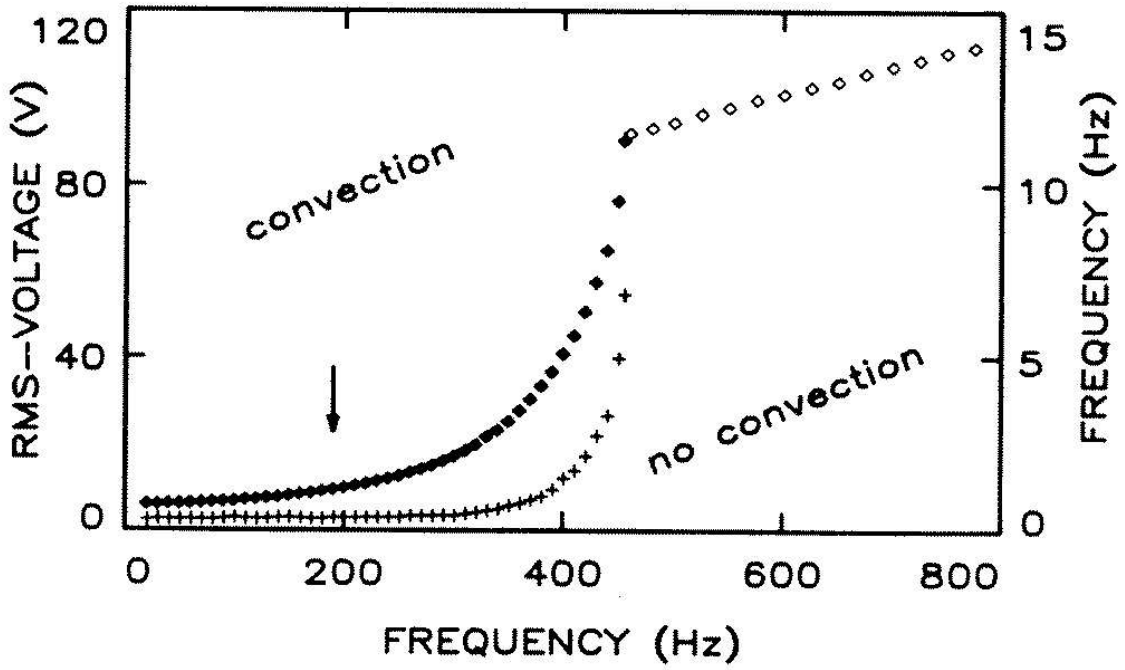

Figure 5.7 Experimental results for a 15 μm cell of MBBA for the Hopf frequency (crosses) and the threshold voltage (solid diamonds for the conductive regime and open diamonds for the dielectric regime). The figure is taken from Ref. [41] (Courtesy of I. Rehberg).

to the stronger condition $\tilde{r} < 0.1$ ($\tau_{\rm rec} > 3$s), and supports this assumption. At f_0 =190 Hz ($\omega_0\tau_q = 1.1$), the measured Hopf frequency $\omega_H/(2\pi)$ was 0.345 Hz. Fitting $\sqrt{\mu_\perp^+\mu_\perp^-}$ in the WEM prediction (5.52) leads (at 25°C) to

$$\sqrt{\mu_\perp^+\mu_\perp^-}^{(MBBA)} = 1.6 \times 10^{-10}\mathrm{m}^2/(\mathrm{Vs}), \tag{5.54}$$

consistent with the values given in Table 3.1.

Figure 5.8 shows the WEM prediction for the Hopf frequency as function of the external frequency for the above mobilities and a vanishing recombination rate. The comparison with the measured values of Fig. 5.7 shows nearly a quantitative agreement. Note, that once $\sqrt{\mu_\perp^+\mu_\perp^-}$ is fixed, all other points of the theoretical curve are determined by the known SM parameters (Appendix A.1).

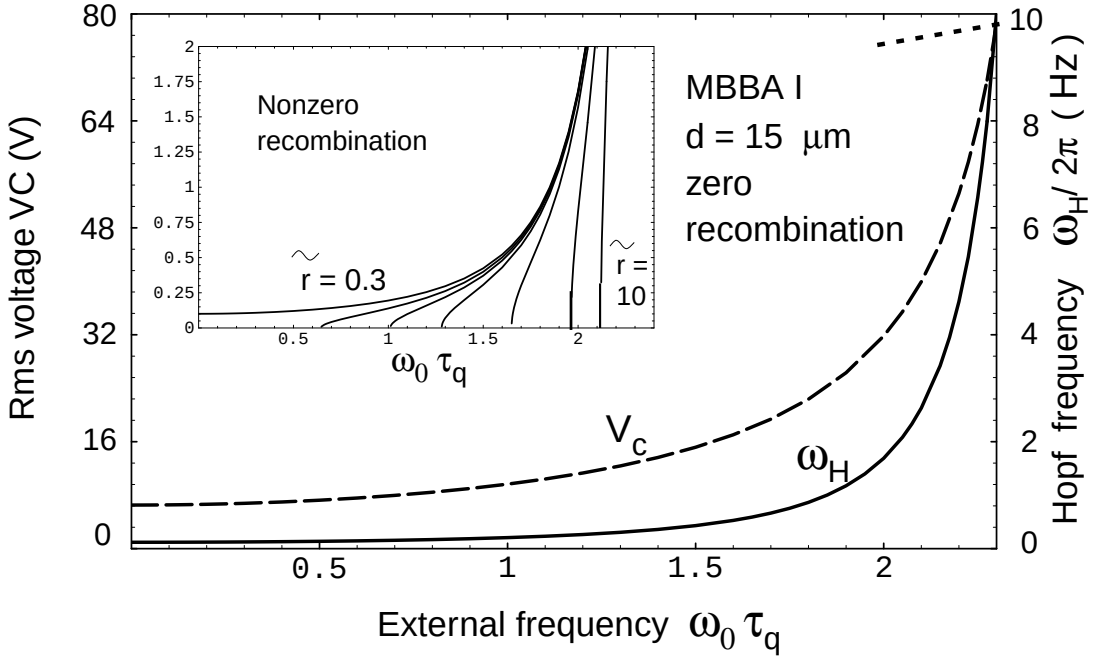

Figure 5.8 Hopf frequency (solid lines) and threshold voltage (dashed) as function of the external frequency for a MBBA cell with the parameters of Ref. [41] (parameter set MBBA I, Appendix A.1 with $\sigma_\perp = 4 \times 10^{-8}(\Omega\mathrm{m})^{-1}$ and $d = 15\ \mu$m), to be compared with Fig. 5.7. Shown is the whole conductive regime. The experimental crossover to the dielectric mode at $\overline{V}_c \approx 80V$ is shown schematically as dash-pointed line (it is not calculated). The scaled frequency $\omega_0\tau_q = 1.1$ (vertical arrow) corresponds in physical units to about 190 Hz (vertical arrow in Fig. 5.7). In the main plot, a negligible recombination rate (in fact $\tilde{r} < 0.3$), is assumed and the geometric mean of the mobility is fitted to the measured Hopf frequency [41] of 0.34 Hz at $\omega_0/2\pi = 190$ Hz ($\omega_0\tau_q = 1.1$) with the result $(\mu_\perp^+\mu_\perp^-)^{1/2} = 1.6 \times 10^{-10}\mathrm{m}^2/(\mathrm{Vs})$. The inset shows the effect of a nonzero recombination while the other parameters are unchanged. The recombination parameter is, from left to right, $\tilde{r} = 0.3, 0.5, 0.7, 1, 2, 5$, and 10. The curve for $\tilde{r} = 0.3$ can be hardly distinguished from that for $\tilde{r} = 0$.

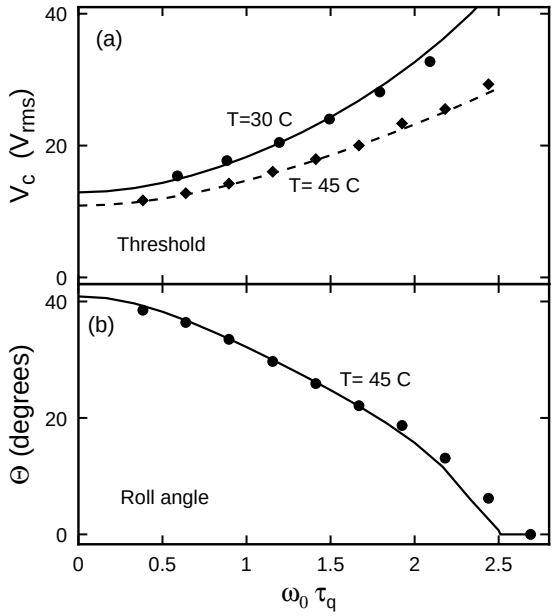

Figure 5.9 Threhold voltage $\overline{V}_c$ and angle Θ of the wavevector with respect to the director, as a function of the dimensionless applied frequency $\omega_0\tau_q$ for the I 52 experiments of Ref. [42]. (a) $\overline{V}_c$ for $T = 30°$C (circles, solid line) and 45°C (diamonds, dashed line). The symbols (lines) are the experimental (theoretical) result. The $\omega_0\tau_q \to 0$ limit is used to determine the temperature dependence of $\sigma_a/\sigma_\perp$, given in the Appendix (A.1). (b) Θ for $T = 45°$C. The temperature dependence of Θ is relatively weak.

5.5.2 Travelling oblique rolls in I 52

The NLC I 52 is more stable than MBBA and the drift in time of the material parameters (especially the conductivity) is slow compared to MBBA or Phase 5 [78]. This enables quantitative measurements at different temperatures. Since $\sigma_\perp$, the viscosities, and ϵ_a have a rather strong temperature dependence, one obtaines qualitatively different Hopf-frequency curves (as function of the external frequency) for different temperatures. Provided that the temperature dependence of the material parameters is known, one can test the WEM on several curves without introducing new unknown parameters.

The experiments were performed by Dennin, Ahlers, and Cannell with cells of 28 μm and 57 μm thickness for six different temperatures [42, 30, 31]. In contrast to MBBA, the bifurcation is to oblique rolls, apart from very high external frequencies (Fig. 5.9). Unfortunately, the relative conductivity anisotropy $\sigma_a(T)/\sigma_\perp(T)$, two elastic constants, and three viscosities, are not known for I 52. They were fitted to the threshold curves and the curves of the roll angle for all six temperatures. Typical examples of the fits are shown in Fig. 5.9.

Eq. (5.52) predicts $\tilde{\omega} \propto \sigma_\perp^{-1/2} d^{-3}$. If $\tilde{\omega} > 2|\lambda_\sigma|$, this is approximately valid for the Hopf frequency as well. Figure 5.10 compares results from the 28 μm cell with that from a 57 μm thick cell of slightly different conductivity, both at 50°C. We find the expected scaling with d for high values of ω_0 where, indeed, $\tilde{\omega} > 2|\lambda_\sigma|$

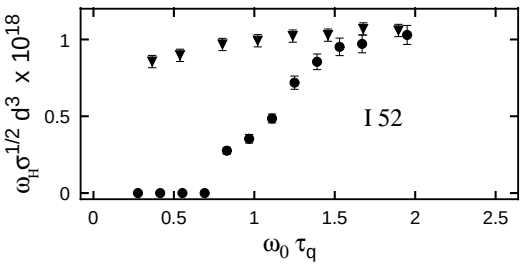

Figure 5.10 $\omega_H\sigma^{1/2}d^3$ as a function of $\omega_0\tau_q$ for one cell of thickness $d = 28$ μm and $\sigma_\perp = 8.5\times10^{-9}$ ohm^{-1} m^{-1} (triangles) and one with $d = 57$ μm and $\sigma_\perp = 1.1\times10^{-8}$ ohm^{-1} m^{-1} (circles) taken from Ref. [42]. Both cells were at $T = 50$°C. For high frequencies the data scale as predicted by the WEM: $\omega_H \propto \sigma^{-1/2}d^{-3}$. The sharp decrease in ω_H as ω_0 is decreased for the thicker cell is predicted by the WEM and fixes the unknown recombination rate.

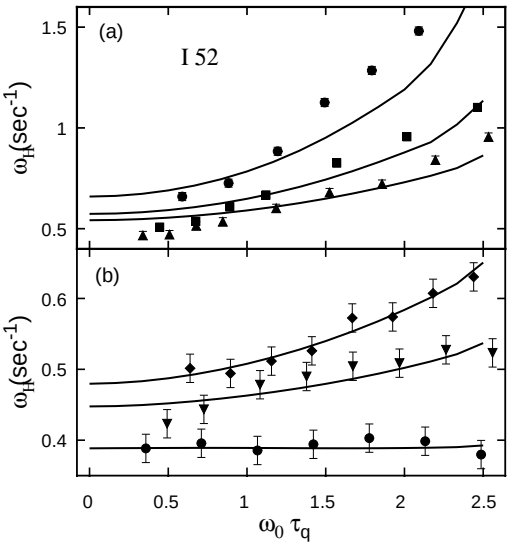

Figure 5.11 Measured and calculated values of the Hopf frequency ω_H as a function of $\omega_0\tau_q$. (a) is for $T = 30$ (circles), 35 (squares), and 40°C (triangles). (b) is for $T = 45$ (diamonds), 50 (triangles), and 60°C (circles). The corresponding results for the WEM model are shown by the solid lines. In both (a) and (b), the abrupt change of slope in the theoretical curves corresponds to the Lifshitz point.

(which can be shown *a posteriori* after determining λ_σ). While $\sigma_\perp^{1/2}d^3$ differs by a factor of 9.6 between the two cells, the product $\omega_H\sigma_\perp^{1/2}d^3$ differs by less than 10 % for high values of ω_0. The relaxation rate $\tau_{\rm rec}^{-1}$ can be found with the help of Eq. (5.53) by identifying for the thick cell (index 1) $\tau_{rec,1}^{-1} = \tilde{\omega}_1^{\rm phys}$ at the external frequency where the Hopf frequency goes to zero ($\omega_0\tau_q = 0.7$ in Fig. 5.10). Since $\omega_{H,2}^{\rm phys} \approx \tilde{\omega}_2^{\rm phys} = 9.6\tilde{\omega}_1^{\rm phys}$ for the thin cell (index 2), the recombination rate can be determined by measuring the Hopf frequency of the thinner cell at the same scaled external frequency, $\tau_{\rm rec} = 1/\tilde{\omega}_1^{\rm phys} = 9.6/\tilde{\omega}_2^{\rm phys} \approx 20$s. Presumably, the recombination rate does depend only on the temperature and not on the cell thickness, so this is the recombination rate for both cells.

Fig. 5.11 shows the measured and predicted Hopf frequencies for a thin $d = 28$ μm cell as function of the external frequency with six temperatures as parameter. The

relaxation time calculated above corresponds to $\tilde{\omega}/|\lambda_\sigma| > 3$ for any temperature and external frequency, so the theoretical $\omega_H \approx \tilde{\omega}$ is computed using Eq. (5.53) with only one adjustable parameter, $\sqrt{\mu_\perp^+ \mu_\perp^-}$, for each temperature. The fitted values increased monotonically with T and were all in the range (see Table A.2)

$$\sqrt{\mu_\perp^+ \mu_\perp^-}^{(I52)} = (0.40...0.47) \times 10^{-10} \mathrm{m}^2/(\mathrm{Vs}), \tag{5.55}$$

The discrepancy (up to 15%) at the lower temperatures (Fig. 5.11a) is related primarily to experimental uncertainties in the very small measured conductivity. For most of the data, experiment and theory agree to within 5% of ω_H.

The WEM captures a number of features of the experiment which are independent of the uncertainties in the material parameters. Both in the model and the experiment, the ω_0 dependence of ω_H is determined mostly by ϵ_a. For $\epsilon_a < 0$ ($T < 60°\mathrm{C}$), ω_H increases with ω_0, and for $\epsilon_a \approx 0$ ($T = 60°\mathrm{C}$), it is essentially constant (Fig. 5.11). In addition, the model predicts $\omega_H \propto \sigma_\perp^{-1/2} d^{-3}$. The correct dependence on temperature in Fig. 5.11 reflects the $\sigma_\perp^{-1/2}$ scaling. Note that $\sigma_\perp$ varies by a factor of 5 over the temperature range $30°\mathrm{C} \leq T \leq 60°\mathrm{C}$. Fig. 5.10 shows the correct d^{-3} scaling for two cells with a ratio of d^3 of about 8. The decrease of ω_H to zero for the thicker cells is predicted by the WEM as well. It fixes the recombination rate. Since, to my knowledge, there are no independent quantitative measurements of τ_{rec}, this last aspect can be considered only as a qualitative agreement. Further work is needed to test the theory in this regime since (in contrast to MBBA) an extremely fine tuning of τ_{rec} is required to match the experiment. This is the result of the nearly vanishing dielectric anisotropy.

5.6 Comparison with other systems showing a Hopf bifurcation

I rely on intuition

A. Einstein

A characteristic feature of the WEM is the interplay between a primary instability mechanism and a slower stabilizing mechanism as shown in the top row of Fig. 5.12. A negative director bend $-iq\delta n_z$ leads *via* $\sigma_a^{(\mathrm{eff})}$ to a charge accumulation $\delta\rho$ and to an electric volume force driving the fluid motion $\delta \boldsymbol{v}$. The orientational viscosities close the destabilizing feedback loop by coupling back velocity gradients to the director bend. The gradients of the charge accumulation, however, excite also the charge-carrier mode whose feedback tends to decrease the charge. This second

mechanism is only relevant if the σ mode can build up, i.e., the relaxation of this mode (symbolically shown by the arrow with the broken line in the diagram in the top row of Fig. 5.12) is slow.

As shown in Fig. 5.12 for three systems of thermal convection, this interplay seems to be a common scenario for generating travelling waves by a Hopf bifurcation The primary destabilizing mechanism in all three systems is that of the "classical" Rayleigh–Bénard convection for isotropic one-component fluids. The buoyancy force of a volume element of hotter fluid ($\delta\theta > 0$) acts as driving force for the fluid motion $\delta\boldsymbol{v}$ which, in turn, advects this element into colder regions thus increasing the relative temperature difference and the buoyancy force.

In thermal convection in a homeotropically aligned NLC cell (second row in Fig. 5.12), the fluid motion excites, in addition, a director distortion δn_x. If the anisotropy of the thermal conductivity is positive (which is nearly always the case), this leads to a positive divergence of the thermal heat flux in the warmer region, i.e., to a cooling of this region corresponding to a stabilizing feedback [99, 61]. The relaxation time of the director is larger than that of the fluid and the temperature by factors of $\tau_{visc}/\tau_d \approx 10^6$, and $P\tau_{visc}/\tau_d$, respectively (P is the Prandtl number and τ_d is defined analogously as in the planar geometry).

In the "thermohaline" convection experiments in salt water (third row in Fig. 5.12), the BC are such that in the basic state, besides the imposed temperature gradient, there is a gradient of the salt concentration with a higher salt concentration near the bottom [100]. So, the fluid element is not only transported into colder regions increasing the relative temperature difference and the buoyancy caused by thermal expansion, but also transported to regions of a lower salt concentration increasing the relative salt concentration and leading to a negative contribution of the buoyancy (the density of the fluid increases with the salt concentration). The time scale of the concentration field is set by the molecular diffusion time $\tau_D = d^2/D$ of the salt concentration (where D is the diffusion coefficient), which is very long compared to other time scales (note that neglect of molecular diffusion, as done in this chapter for the charge carriers, corresponds to an infinitely long diffusion time).

At last, the bottom row of Fig. 5.12 shows thermal convection in a binary mixture of fluids for the case where the Soret effect leads to a negative separation ratio ψ [22, 54, 9], i.e., temperature inhomogenities induce a mass flux $\propto \psi\boldsymbol{\nabla}T$ of the more dense component, which is directed towards the warmer regions. The BC of impenetrable walls together with the imposed temperature gradient lead in the basic state to a linear concentration profile where the concentration of the heavier fluid component decreases with z. The stabilizing concentration mode [101] is excited in

two ways, i) by advection through the concentration gradient of the basic state, as in the thermohaline system; ii) directly by the Soret effect where the temperature inhomogeneity of the linear mode induces a flux of the more dense component into the warmer regions. The time scale of the concentration mode is governed by the concentration diffusion time τ_D, related to the thermal diffusion time $\tau_{th} = d^2/\kappa$ (κ is the thermal diffusion coefficient) by the "Lewis number" $\mathcal{L} = \tau_{th}/\tau_D$ which is $\approx 10^{-2}$ or smaller for liquid mixtures.

The parameters $-\psi$ and $\mathcal{L}$ are, in some way, the analog of $\tilde{\alpha}$ and $\tilde{r}$ in the WEM. The excitation of the concentration mode (of the WEM carrier density mode) is proportional to $-\psi$ ($\tilde{\alpha}^2$), while its relaxation is proportional to $\mathcal{L}$ ($\tilde{r}$). A Hopf bifurcation occurs if $\sqrt{-\psi} > c_1\mathcal{L}$ ($\tilde{\alpha} > c_2\tilde{r}$) with c_1, c_2 of the order of unity, and if the condition is well satisfied (and $\sqrt{-\psi} <\approx 0.3$), the Hopf frequency is $\propto \sqrt{-\psi}$ ($\propto \tilde{\alpha}$); see, e.g., Fig. 5.2. in Ref. [9] for binary mixtures. In contrast to the WEM, the interesting parameter ranges near the codimension-two curve or near the tricritical curve are, at least for usual liquid mixtures, extemely narrow (typically, $0 > \psi \geq -10^{-4}$) and therefore experimentally hard to attain.

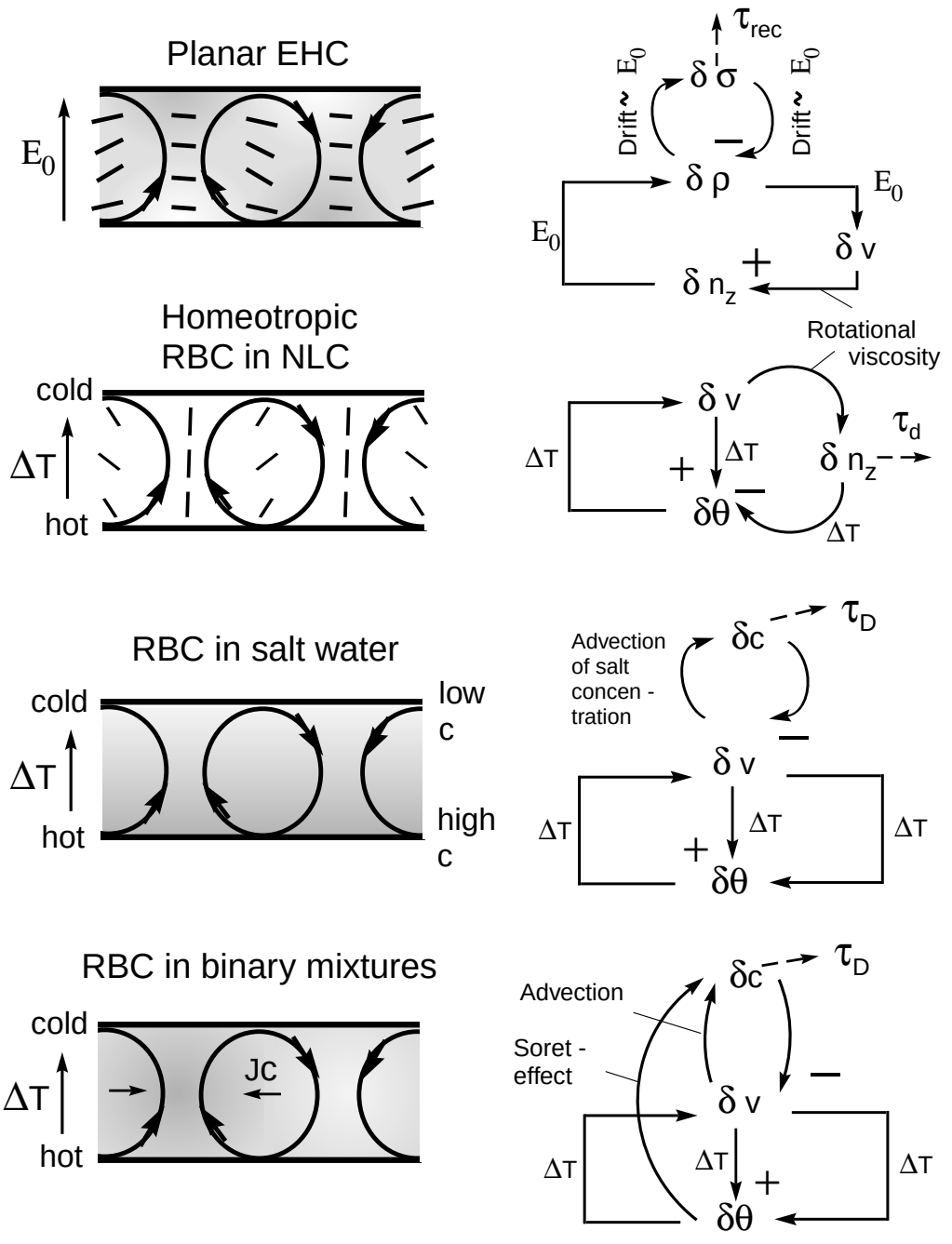

Figure 5.12 Comparison of the WEM mechanism to that of three Rayleigh–Bénard systems which also show a Hopf bifurcation, at least in certain parameter ranges. In each case, the basic destabilizing feedback cycle (straight lines) is coupled to a stabilizing one with a slower time scale (curved lines). The time scale of the stabilizing fields due to relaxation is indicated by arrows with a broken line. In each example, the physical effects providing the coupling to the stabilizing cycle is given. The symbols E_0 or ΔT indicate that the corresponding effect of one field onto the next is proportional to the external driving.